Wang *et al. Energy Mater.* **2025**, *5*, 500008
DOI: 10.20517/energymater.2024.87

Energy Materials

Article

Open Access

Check for updates

Efficient and stable lithium storage of porous carbon fiber composite bimetallic sulfides (FeS-ZnS) anode

Wei Wang[1], Huichuan Tang[1], Joao Cunha[2], Maryam Karimi[2], Najeeb Lashari[2], Aqrab Ahmad[2], Hong Yin[1,2,*]

[1]Key Laboratory of Hunan Province for Advanced Carbon-Based Functional Materials, School of Chemistry and Chemical Engineering, Hunan Institute of Science and Technology, Yueyang 414006, Hunan, China.
[2]International Iberian Nanotechnology Laboratory (INL), Av. Mestre Jose Veiga, Braga 4715-330, Portugal.

***Correspondence to:** Dr. Hong Yin, Key Laboratory of Hunan Province for Advanced Carbon-Based Functional Materials, School of Chemistry and Chemical Engineering, Hunan Institute of Science and Technology, No. 439, Xiangbei Road, Yueyanglou District, Yueyang 414006, Hunan, China. E-mail: hong.yin@inl.int

How to cite this article: Wang, W.; Tang, H.; Cunha, J.; Karimi, M.; Lashari, N.; Ahmad, A.; Yin, H. Efficient and stable lithium storage of porous carbon fiber composite bimetallic sulfides (FeS-ZnS) anode. *Energy Mater.* **2025**, *5*, 500006. https://dx.doi.org/10.20517/energymater.2024.87

Received: 24 Jul 2024 **First Decision:** 21 Aug 2024 **Revised:** 6 Sep 2024 **Accepted:** 26 Sep 2024 **Published:** 7 Jan 2025

Academic Editor: Yuping Wu **Copy Editor:** Fangling Lan **Production Editor:** Fangling Lan

Abstract

To enhance the utilization of lithium-ion battery anodes, it is crucial to improve both the lithium storage stability and kinetics of transition metal sulfides. This optimization is critical for the development of battery technologies that are more efficient, durable, and environmentally sustainable. In this study, a facile electrospinning technique followed by a thermal treatment was used to fabricate a bimetallic sulfide/porous carbon fiber composite (FeS-ZnS/PCFs). Its stability was largely improved due to the buffered ability derived from its porous structure. The presence of FeS-ZnS grain boundaries fosters the generation of extra redox active sites, ultimately boosting the kinetics of lithium storage. The optimized composite material exhibits excellent stability and efficient lithium storage performance. Density functional theory calculations and kinetics analysis further clarify superior lithium storage capabilities of this material.

Keywords: Bimetallic sulfides, carbon fibers, porous structure, electrospinning, lithium-ion battery

INTRODUCTION

The rising necessity for lithium-ion batteries (LIBs) in electronic gadgets and electric vehicles calls for

improved energy and power density, as well as enhanced cycle durability. Nevertheless, advancements in anode materials for LIBs have lagged behind that of cathode materials, ultimately obstructing the overall progress of LIBs[1-3]. The deficit of the regular graphite anodes, especially regarding theoretical specific capacity and rate performance, underlines the necessity to consider other anode materials[4-6]. One of the most attractive alternate materials is the compound zinc sulfide (ZnS), which reaches a remarkable theoretical capacity of 962.0 mAh g^{-1}[7]. Furthermore, ZnS has some other strengths: first, it is found quite easily in nature, and second, it can be produced through rather simple means of synthesis[8-10].

However, one of the main complaints about ZnS is the weakness of its electrical conductivity, which can result in polarization during lithium storage processes. Moreover, the volume variation in lithium storage cycles may cause a rapid decrease in capacity. Hence, it is crucial to employ effective optimization techniques to address these problems efficiently. Wang *et al.* utilized electrospinning to produce ZnS composite porous carbon fiber materials[11]. The unique porous structure of the material effectively mitigates the volume expansion of ZnS nanoparticles throughout lithium storage cycles, thereby ensuring exceptional stability. Additionally, Zhang *et al.* synthesized ZnS/SnS@C yolk-shell microspheres (ZSS@NC) using a combination of hydrothermal processing, polypyrrole (PPy) coating, and microsphere sulfidation strategies[12]. The material exhibited a consistent specific capacity of 571.2 mAh g^{-1} after experiencing 1,000 cycles at a current density of 1 A g^{-1}. The optimization of morphology and structure is key to enhancing the lithium storage performance of composites[13]. Therefore, employing multi-metal compounds and the construction of composite and porous structures have emerged as promising strategies[14,15]. Contrary to the generally accepted view that heterophase interfaces could hinder electronic transfer and cause interface polarization[16,17], multi-metal sulfides within a polycrystalline structure can produce multiple active sites at grain boundaries and synergistic effects. Therefore, the reversible capacity of the material is increased, supporting effective charging and discharging operations. Guan *et al.* developed novel hydrangea-like hierarchical $Zn_{0.76}Co_{0.24}S$@NC@MoS_2, termed ZCS@NC@MS[18]. The N-doped carbon framework in this material serves to enhance electrical conductivity and reduce volume expansion effects. Additionally, the heterointerfaces play a crucial role in inducing a built-in electric field, thereby promoting ion diffusion kinetics. The material maintains a specific capacity of 680.0 mAh g^{-1} after 1,000 cycles at a current density of 1 A g^{-1}. Notably, the lithium insertion/extraction reactions of multi-metal components occur at varying voltages, displaying a stepwise lithium storage phenomenon akin to tin-antimony alloys[19]. This mechanism could offer structural buffering through the facilitation of asynchronous lithium storage[2]. Additionally, the incorporation of porous structures can facilitate electrolyte diffusion at material interfaces and within the bulk[20], necessitating its inclusion in material design considerations. He *et al.* developed MoS_2 nanoflowers on N-doped hollow multi-nanochannel carbon nanofibers[13]. By leveraging the hollow, multi-nanochannel architecture to withstand significant internal strain and volume fluctuations during cycling, they achieved outstanding lithium storage performance.

This work utilized the surplus sulfur content in zinc diethyldithiocarbamate (ZDEC) for sulfur and zinc, along with iron acetylacetonate for iron, to successfully synthesize bimetallic sulfides (FeS-ZnS) in a single step. Using polyacrylonitrile (PAN) as the electrospinning substrate and poly(ethylene oxide)-poly(propylene oxide)-poly(ethylene oxide) copolymer (Pluronic P123) as the soft template, bimetallic sulfide/porous carbon fiber (FeS-ZnS/PCFs) composite materials were fabricated through a straightforward electrospinning technique followed by a calcination process. The effective mixing of two different metal sulfides leads to enhanced lithium storage performance through synergistic effects and increased site availability. Furthermore, the asynchronous lithium storing of multi-metal components efficiently reduces structural strain. The proposed methodology for designing and preparing materials in this study offers valuable insights to improve the efficacy of lithium storage materials that contain transition metal sulfides.

EXPERIMENTAL

Materials

In this experiment, analytical grade chemicals were used without any further purification. Zinc diethyl dithiocarbamate (ZDEC), ferric acetylacetonate, PAN, N-dimethylformamide (DMF), and N-methyl-2-pyrrolidone (NMP) were sourced from Aladdin Reagent Co., LTD., China. The ploy(ethylene glycol)-block-poly(propylene glycol)-block-poly(ethylene glycol) copolymer (Pluronic P123) was supplied by Sigma-Aldrich Co., LTD., Germany.

Preparation of FeS-ZnS/PCFs

Initially, 1 g of PAN and 1.5 g of Pluronic P123 were combined in a 10 mL solvent (DMF and NMP in a 1:1 volume ratio) and thoroughly stirred at 45 °C. Subsequently, 1.6 g of ZDEC and 0.388 g of ferric acetylacetonate (with a molar ratio of 4:1) were added to the mixture, which was stirred for 12 h at 45 °C. Electrospinning was then carried out at a voltage of 19 kV, with a nozzle-to-substrate distance of 20 cm and a constant flow rate of 0.1 mL h^{-1}. The resulting precursor underwent heat treatment at 250 °C for 2 h in a muffle furnace, followed by a 2-h calcination process in a nitrogen-saturated tube furnace at 600 °C. The resulting product was designated as FeS-ZnS/PCFs-20%. By adjusting the molar ratio of ZDEC and ferric acetylacetonate to 9:1 and 7:3, FeS-ZnS/PCFs-10% and FeS-ZnS/PCFs-30% were obtained, respectively. Besides, samples lacking iron acetylacetonate and any metal salts are referred to as ZnS/PCFs and PCFs, respectively. The sample produced through the direct thermal decomposition of ZDEC is labeled as ZnS/C.

RESULTS AND DISCUSSION

The process of preparing FeS-ZnS/PCFs, as illustrated in Supplementary Figure 1, entails utilizing electrospinning to produce precursors and employing calcination to produce composite materials. PAN functions as the electrospinning substrate, with Pluronic P123 serving as the soft template. Furthermore, ZDEC is used as the sulfur and zinc source while iron acetylacetonate is employed as the iron source. PAN transforms into carbon fibers when it is calcined in a nitrogen atmosphere. At the same time, Pluronic P123 volatilizes and causes pores to grow on the surface of carbon fibers. ZnS particles are synthesized *in situ* on carbon fibers using ZDEC, which has an atomic ratio of 1:4 of Zn to S. As a result, surplus S combines with Fe to form FeS. As a result, as the structural model shows, the resulting FeS-ZnS/PCFs material might have heterointerfaces between FeS and ZnS.

X-ray diffraction (XRD) analysis was conducted to examine the crystallographic characteristics of the composites, as demonstrated in Figure 1A and Supplementary Figure 2. The diffraction peaks observed for FeS-ZnS/PCFs-20% corresponded with the standard reference patterns for wurtzite-type ZnS (PDF#89-2942) and FeS (PDF#86-0389). These results confirm the presence of both ZnS and FeS within the composite materials[21]. The XRD patterns for the other FeS-ZnS/PCFs samples are very similar to those of FeS-ZnS/PCFs-20%. Identifying the diffraction peak on the (002) crystalline plane of carbon in the composite sample was difficult because it slightly overlaps with the ZnS peaks in terms of 2θ position. The content of carbon and metal sulfide in the material was measured by thermogravimetric analysis (TGA). Carbon oxidation is indicated by the weight reduction at 400 °C, as shown in Figure 1B[22]. The peak around 450 °C, followed by a gradual decrease in weight, signifies the oxidation of sulfides[23]. The mass percentage of FeS-ZnS/PCFs-20% maintains at 32.4% above 650 °C. The TGA results for ZnS/PCFs and other FeS-ZnS/PCFs samples are similar, with about 30% mass retention, as shown in Supplementary Figure 3.

To examine the chemical composition and states on the surface of FeS-ZnS/PCFs-20% and ZnS/PCFs composites, X-ray photoelectron spectroscopy (XPS) analysis was conducted. As depicted in Figure 1C, the XPS spectrum of FeS-ZnS/PCFs-20% exhibits[24] characteristic peaks corresponding to Zn 2p, Fe 2p, O 1s, N 1s, C 1s, S 2s and S 2p, whereas the XPS result of ZnS/PCFs [Supplementary Figure 4A] does not show

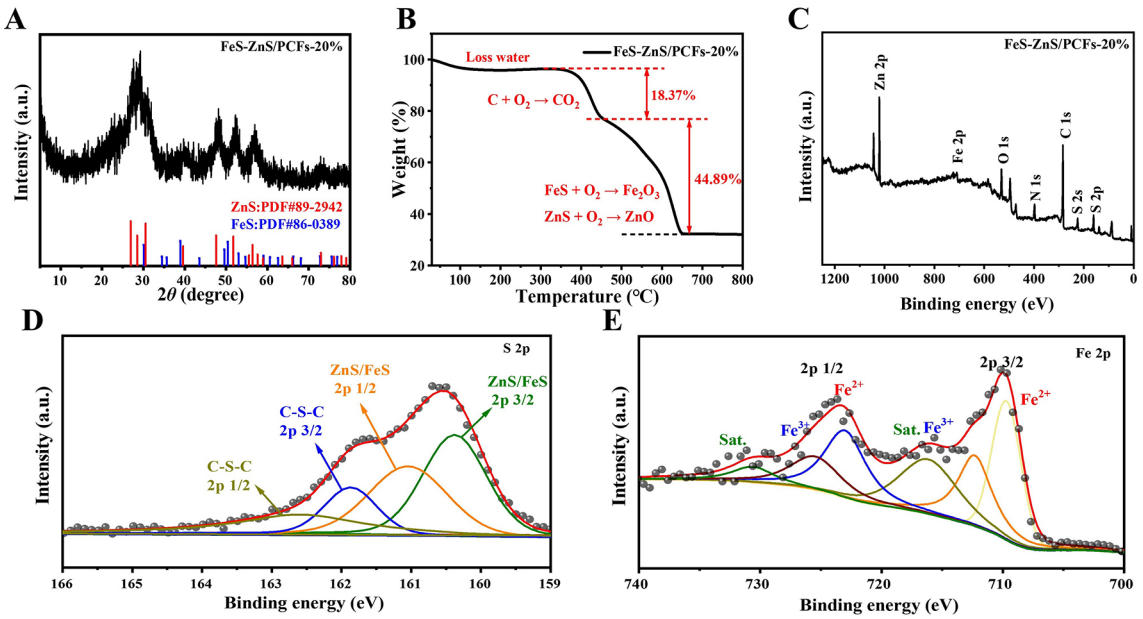

Figure 1. (A) XRD patterns of the FeS-ZnS/PCFs-20% composite; (B) TG curve of the FeS-ZnS/PCFs-20% composite; (C) XPS spectra of the FeS-ZnS/PCFs-20% composite; (D) High-resolution S 2p of the FeS-ZnS/PCFs-20% composite; (E) Fe 2p spectrum of the FeS-ZnS/PCFs-20% composite.

the presence of Fe, indicating the incorporation of a Fe elemental component into FeS-ZnS/PCFs-20%. The two main peaks of the high-resolution spectra of S 2p [Figure 1D] at 160.6 and 160.2 eV, respectively, correspond to S $2p_{1/2}$ and S $2p_{3/2}$ of lattice sulfide (ZnS and FeS), according to the deconvolution analysis[25,26]. The peaks of S 2p spectrum at 161.4 and 161.9 eV are attributed to C-S-C bonds present in carbon-based materials[27]. The high-resolution Zn 2p spectrum depicted in Supplementary Figure 4B reveals peaks at 1,044.58 and 1,021.58 eV, which are indicative of ZnS, aligning with the Zn $2p_{1/2}$ and Zn $2p_{3/2}$ peaks, as reported[28]. FeS-ZnS/PCFs-20%'s Zn 2p high-resolution spectra showed a noticeable positive shift when compared to ZnS/PCFs. Zn $2p_{1/2}$ and Zn $2p_{3/2}$ are represented by the peak binding energies in ZnS/PCFs, which are 1,043.9 and 1,020.8 eV, respectively. This shift indicates that Zn ion electron cloud density in FeS-ZnS/PCFs-20% has decreased, which can be attributed to the natural influence of FeS heterointerfaces[29]. The deconvolution analysis of the Fe 2p high-resolution spectrum [Figure 1E] revealed that the peaks at 723.38 and 709.98 eV correspond to the Fe $2p_{1/2}$ and Fe $2p_{3/2}$ peaks of Fe^{2+}, respectively[30]. Additionally, the distinctive peaks at 725.68 and 712.38 eV are attributed to Fe $2p_{1/2}$ and Fe $2p_{3/2}$ of Fe^{3+}, respectively[31]. The presence of Fe^{3+} is a result of the oxidation of a small quantity of Fe^{2+} on the FeS surface by atmospheric oxygen[32]. The XPS characterization results offer additional support for the successful synthesis of FeS-ZnS/PCFs composites and suggest potential interactions between FeS and ZnS.

With the use of a scanning electron microscope (SEM), the microstructure of materials was analyzed. In Figure 2A, the ZnS/PCFs sample exhibits a configuration characterized by the presence of ZnS nanoparticles dispersed loosely on porous carbon fibers, with the pores on the cross-section of the fibers being distinctly observable. On the other hand, the structure of the FeS-ZnS/PCFs-20% composite, as shown in Figure 2B, indicates the transition metal sulfide nanocrystals are slightly agglomerated. Furthermore, Supplementary Figure 5 shows that a higher ferric acetylacetonate content during preparation leads to a propensity for disorder in the stacking arrangement of sulfide nanocrystals in the composite. The formation of transition metal sulfide nanocrystals does not impede the creation of pore channels in the carbon fibers, as demonstrated by the distinctive porous structure evident in the cross-sections. However, the presence of

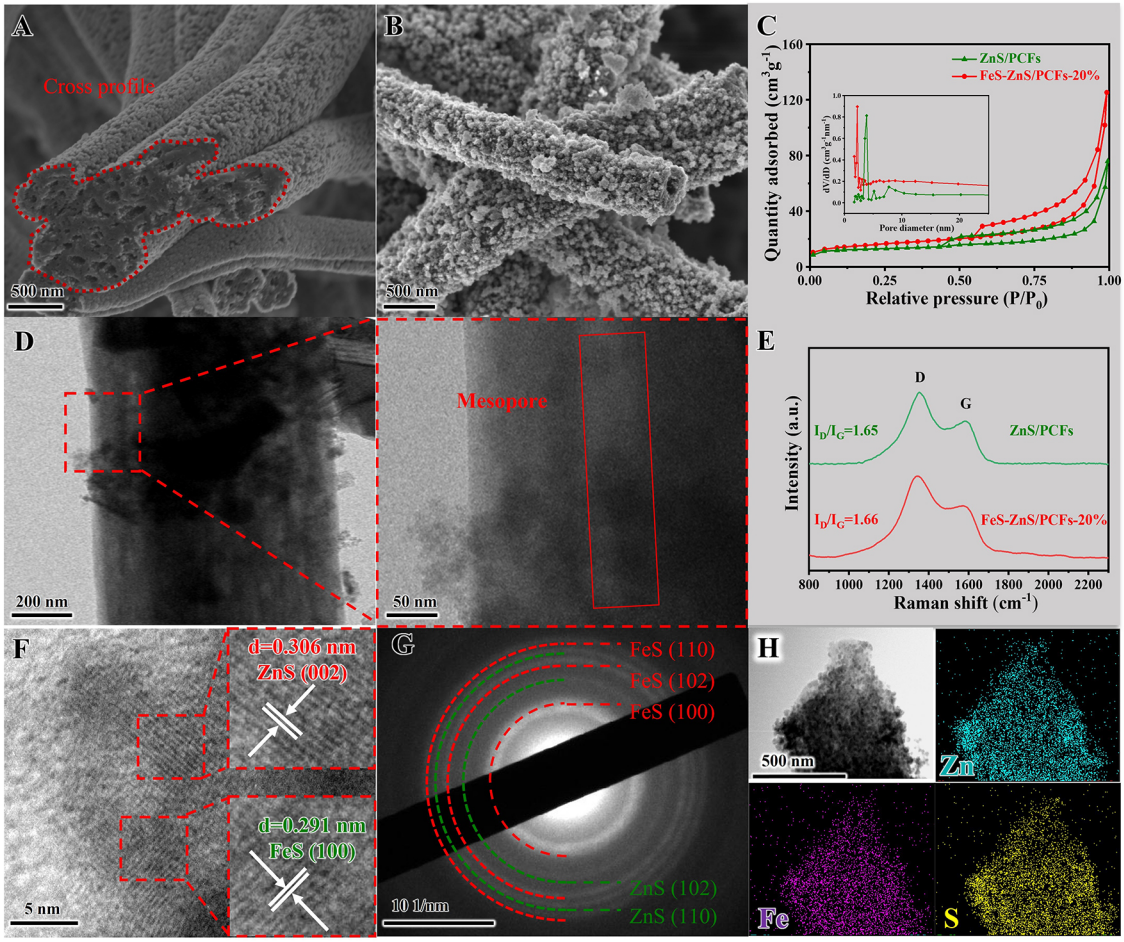

Figure 2. (A) SEM images of ZnS/PCFs; (B) SEM images of FeS-ZnS/PCFs-20%; (C) N_2 adsorption-desorption isotherms with the BJH pore-size distribution of ZnS/PCFs and FeS-ZnS/PCFs-20%; (D) High-magnification TEM image of FeS-ZnS/PCFs-20%; (E) Raman spectra of ZnS/PCFs and FeS-ZnS/PCFs-20%; (F) HRTEM image of FeS-ZnS/PCFs-20%; (G) Selected area electron diffraction (SAED) pattern of FeS-ZnS/PCFs-20%; (H) TEM-EDS mapping image of the FeS-ZnS/PCFs-20%.

transition metal sulfides may influence the porous nature of the material. Following this, an investigation into the specific surface area and pore structure of the samples was performed utilizing nitrogen isothermal adsorption-desorption curves. The isotherms of the ZnS/PCFs and FeS-ZnS/PCFs samples [Figure 2C and Supplementary Figure 6A] demonstrate distinct International Union of Pure and Applied Chemistry (IUPAC) classification type IV characteristics. Additionally, the observation of a H4-type hysteresis loop within a P/P0 range of 0.5-1.0 suggests the existence of mesopores in the composites[33]. The Brunauer-Emmett-Teller (BET) specific surface area of FeS-ZnS/PCFs-20% (55.72 $m^2 g^{-1}$) showed a slight increase compared to that of ZnS/PCFs (47.9 $m^2 g^{-1}$). This indicates that the produced FeS impacted the pore structure of the carbon fibers. The utilization of the Barrett-Joiner-Halenda (BJH) method for pore size distribution curves [Supplementary Figure 6B] has revealed that all samples are mesoporous with predominant pore sizes falling within the 2-5 nm range. However, the FeS-ZnS/PCFs-20% variant displays smaller pores compared to ZnS/PCFs. This result is ascribed to the denser configuration of nanocrystals made of transition metal sulfide, as previously mentioned.

The microstructure of FeS-ZnS/PCFs-20% was extensively examined through the high-resolution transmission electron microscope (HRTEM) technique[34]. Figure 2D clearly demonstrates the distribution

of sulfide nanoparticles on the carbon fibers. The fibers serve as a carbon-based substrate, potentially exhibiting strong inherent interactions with the sulfide nanoparticles. Furthermore, the distinct contrast between bright and dark areas on the carbon fibers serves as proof of the existence of mesoporous channels within the fibers. These channels could potentially hinder the expansion of volume during the storage of lithium. The Raman spectra data presented in Figure 2E and Supplementary Figure 7 indicate a notable resemblance in the high defect ratio I_D/I_G (the intensity ratio of the D peak to the G peak) of the composite. Both values exceed 1.6. The presence of transition metal sulfides alongside carbon fibers appears to create a significant quantity of defect sites, which enhance the adsorption of Li-ions at the surface and interface[35].

Lattice fringes in Figure 2F reveal the (100) crystal plane with a spacing of 0.3331 nm in the ZnS composites[36]. Additionally, a crystal plane spacing of 0.3133 nm is specific to the (111) crystal plane, which is prevalent in FeS[37]. These findings support the conclusions of the XRD analysis. The lack of distinct demarcation between ZnS and FeS particles indicates strong connectivity at the nanocrystalline scale, resulting in the formation of numerous polycrystalline particles. The selected area electron diffraction (SAED) pattern in Figure 2G reveals diffraction rings, characteristic of a polycrystalline structure. However, it does not show clear diffraction spots, indicating a uniform distribution of ZnS and FeS in the FeS-ZnS/PCFs-20% composite[38]. The sizes of the polycrystalline diffraction rings can be utilized to identify that they correspond to the (110), (102), and (100) crystallographic planes of FeS, as well as the (102) and (110) planes of ZnS. The transmission electron microscopy-energy dispersive X-ray spectroscopy (TEM-EDS) mapping of the FeS-ZnS/PCFs-20% composite in Figure 2H demonstrates a substantial convergence in the spatial arrangement of zinc (Zn), iron (Fe), and sulfur (S) elements inside the composite material. This result offers more substantiation for the interconnection of FeS and ZnS at the nanocrystal scale, as opposed to mere blending in the composite. Furthermore, as indicated by the EDS analysis, the zinc-to-iron molar ratio is 3.4:1 [Supplementary Table 1], slightly lower than the initial feed ratio of 4:1. This discrepancy suggests a potential loss of zinc, likely due to its higher sublimation tendency during calcination. Based on the elemental ratios and TGA findings, the sample is found to contain 30.09 wt.% of ZnS and 7.98 wt.% of FeS.

The lithium storage mechanism of the anodes was clarified through the use of galvanostatic charge-discharge (GCD) and cyclic voltammetry (CV). Figure 3A illustrates the GCD curves of the first and fifth cycles for ZnS/PCFs and FeS-ZnS/PCFs-20%. The findings reveal that the initial discharge capacity of FeS-ZnS/PCFs-20% is 1,490.4 mAh g^{-1}, surpassing both ZnS/PCFs (1,022.4 mAh g^{-1}) and FeS-ZnS/PCFs-10% (1,255.5 mAh g^{-1}), and marginally outperforming FeS-ZnS/PCFs-30% (1,445.7 mAh g^{-1}). The main reason for capacity reduction in the first cycle is primarily linked to the development of the solid electrolyte interface (SEI) layer and the degradation of the electrolyte[39]. In addition, the FeS-ZnS/PCFs-20% arrangement has a separate plateau that exceeds 2.5 V while charging, indicating unsynchronized phase transitions in lithium retention[40]. The GCD curves observed for the FeS-ZnS/PCFs-10% and FeS-ZnS/PCFs-30% anodes [Supplementary Figure 8] show resemblances to the GCD curve of the FeS-ZnS/PCFs-20% anode. Figure 3B and C displays the CV curves for ZnS/PCFs and FeS-ZnS/PCFs-20%, respectively. The peaks observed at approximately 0.3-0.4 V in the initial CV scan are attributed to the development of the surface SEI for the active material[41]. A reduction peak between 0.5 and 1.0 V indicates the phase transition between Li-ions and transition metal sulfides ($FeS + 2Li^+ + 2e^- \rightarrow Fe + Li_2S$[42]; $ZnS + 2Li^+ + 2e^- \rightarrow Zn + Li_2S$[43]). The reductive peak of FeS-ZnS/PCFs-20% exhibits more prominence, indicating its higher reactivity in comparison to ZnS/PCFs. During the positive scan, the FeS-ZnS/PCFs-20% sample exhibits a wide oxidation peak spanning from 1.0 to 1.7 V, along with an additional oxidation peak at 2.7 V. The results suggest that the existence of FeS enhances a cooperative interaction between ZnS and FeS, hence increasing the reactivity during the entire process[44]. The material has exceptional reversibility, as indicated by the great repeatability observed in the CV curves after the initial cycle. This suggests that the FeS-ZnS/

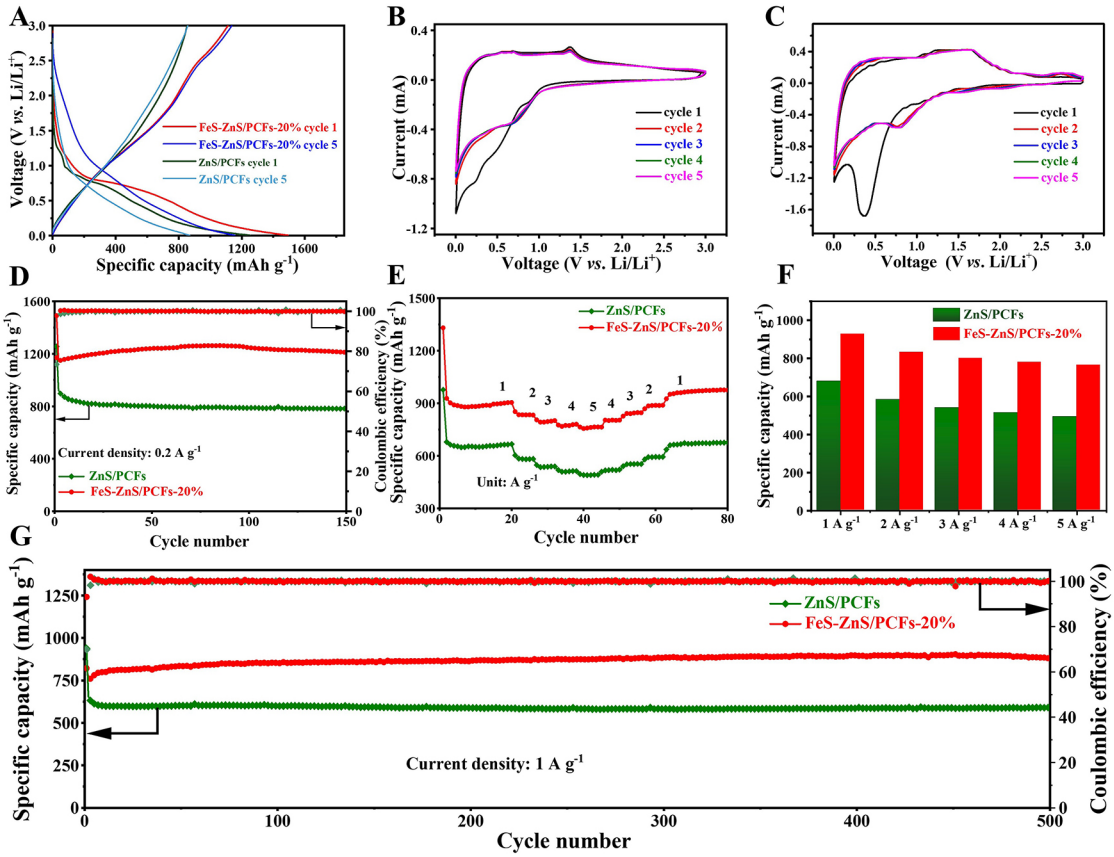

Figure 3. (A) 1st, 5th GCD profiles of the FeS-ZnS/PCFs-20% anode at 0.2 A g^{-1}; (B) CV curves of the ZnS/PCFs anode at 0.5 mV s^{-1}; (C) CV curves of the FeS-ZnS/PCFs-20% anode at 0.5 mV s^{-1}; (D) Cycling performance of ZnS/PCFs and FeS-ZnS/PCFs-20% anodes at 0.2 A g^{-1}; (E) Rate performance of the ZnS/PCFs and FeS-ZnS/PCFs-20% anodes at different current densities of 1, 2, 3, 4 and 5 A g^{-1}; (F) Capacity histograms of ZnS/PCFs and FeS-ZnS/PCFs-20% anodes; (G) Long cycling performance of the anodes at 1 A g^{-1}.

PCFs-20% anode is capable of undergoing lithiation-delithiation cycles multiple times without undergoing substantial deterioration, making it a very desirable characteristic in LIBs. In general, the data above suggest that FeS has the ability to initiate non-synchronous phase transitions in lithium storage, resulting in a significant reduction in structural strain[45].

As shown in Figure 3D, FeS-ZnS/PCFs-20% exhibits a high discharge specific capacity of 1,208.9 mAh g^{-1} after 150 cycles at a current density of 0.2 A g^{-1}. This value is considerably greater than that of ZnS/PCFs. Notably, the specific capacity of FeS-ZnS/PCFs-20% shows a modest rise as the cycle continues. The observed behavior, as well as the high lithium storage capacity of the material, can be attributed to the synergistic interaction between ZnS and FeS. This interaction leads to a more active redox reaction with Li-ions and an increase in the ability of the material to store lithium by interfacial adsorption[46]. While the discharge specific capacity of the FeS-ZnS/PCFs-10% and FeS-ZnS/PCFs-30% anodes is lower than that of the FeS-ZnS/PCFs-20% anode, it is still higher than that of the ZnS/PCFs anode, as shown in Supplementary Figure 9A. Figure 3E displays the rate performance of FeS-ZnS/PCFs-20% and ZnS/PCFs. For FeS-ZnS/PCFs-20%, its discharge capacity is 904.5 mAh g^{-1} at a current density of 1 A g^{-1}. Notably, even at a higher current density of 5 A g^{-1}, the discharge capacity can also achieve 763.9 mAh g^{-1}. When the current density reverts to 1 A g^{-1}, the capacity increases to 975.2 mAh g^{-1}, which exceeds that of ZnS/PCFs. Figure 3F displays capacity histograms of ZnS/PCFs and FeS-ZnS/PCFs-20% anodes at varying current densities. Additionally, Supplementary Figure 9B compares the reversible capacity retention of ZnS/PCFs

and FeS-ZnS/PCFs-20% at different speeds. As current density rises, the reversible capacity retention diminishes owing to polarization. However, the presence of heterointerfaces in FeS-ZnS/PCFs-20% facilitates rapid Li-ion insertion and extraction, leading to superior retention of reversible capacity compared to ZnS/PCFs. At a high current density of 5 A g^{-1}, FeS-ZnS/PCFs-20% exhibits a reversible capacity retention of 82.35%, surpassing the 72.43% retention of ZnS/PCFs. The electron transfer occurring between ZnS and FeS at their interface facilitates the adsorption of Li-ions on the interface and surface of FeS-ZnS/PCFs-20%, leading to enhanced lithium storage capacity[47]. Clearly, FeS-ZnS/PCFs-20% has exceptional rate performance. The anodes FeS-ZnS/PCFs-10% and FeS-ZnS/PCFs-30% [Supplementary Figure 9C] demonstrate exceptional rate performance due to the synergistic impact coming from the interconnected interfaces between ZnS and FeS. Supplementary Table 2 presents a comparison of the mean specific capacities of the samples at various current densities in order to provide a clearer representation of this pattern. The results suggest that the material has higher surface/interface activity, which helps to speed up the processes of lithiation and delithiation[48].

The durability of ZnS/PCFs and FeS-ZnS/PCFs-20% anodes under a current density of 1 A g^{-1} is evidenced in Figure 3G. The FeS-ZnS/PCFs-20% anode surpasses the ZnS/PCFs anode, demonstrating a significant discharge capacity of 881.9 mAh g^{-1} after 500 cycles. Similarly, the anodes of FeS-ZnS/PCFs-10% and FeS-ZnS/PCFs-30% exhibit improved long-term cycling capacities compared to ZnS/PCFs, as shown in Supplementary Figure 9D. Additionally, as depicted in Supplementary Figure 10, PCFs show good stability, albeit with a lower lithium storage capacity, whereas ZnS/C also exhibits inferior lithium storage performance in comparison to the composite material. The remarkable lithium storage capacities demonstrated by the FeS-ZnS/PCFs-20% anode can be explained by three main factors. The synergistic effect of FeS and ZnS enhances the redox activity of the material, facilitating the lithiation-delithiation processes[40]. Furthermore, the inclusion of various transition metal sulfide components in the design allows for separate storage of lithium, effectively reducing the impact of structural strain[2]. Finally, the grain boundaries of multi-transition metal sulfides provide many active sites, which enhance electron transport and the adsorption of Li-ions at interfaces. This improves the amount of charge that can be stored and allows for fast charging and discharging abilities[49]. Hence, the FeS-ZnS/PCFs-20% anode demonstrates a significant superiority in terms of lithium storage capacity when compared to current ZnS-based investigations, as depicted in Table 1.

For a deeper understanding of the exceptional ability of FeS-ZnS/PCFs-20% to store lithium, we employed density functional theory (DFT) and conducted investigations on the kinetics of lithium storage. The extra information provided an explanation of the procedures used to distinguish the composite materials. Figure 4A and B depicts the crystal structures of ZnS and FeS, respectively. The composite models shown in Figure 4C consist of a combination of single-layer graphene with a ZnS cluster ($Zn_{32}S_{33}$) for ZnS/PCFs[52], and a combination of a ZnS cluster ($Zn_{17}S_{18}$) and an FeS cluster ($Fe_{10}S_{11}$) for FeS-ZnS/PCFs[53]. The charge density difference result of FeS-ZnS/PCFs model indicates significant charge transfer taking place at the FeS-ZnS contact. The red and blue regions on the diagram signify electron gain and loss, respectively. The findings align with the observed change in binding energy of Zn in previous XPS investigations, suggesting that the combined effect of FeS and ZnS promotes the transfer of charges, hence enhancing the movement of Li-ions at the interface[40]. In addition, the density of states (DOS) for both models was determined by normalizing and setting the Fermi energy to 0 eV. As seen in Figure 4D, the DOS in the FeS-ZnS/PCFs model exhibits a modest increase. This is attributed to the greater abundance of d orbitals in close proximity to the Fermi energy, in contrast to the ZnS/PCFs model. This phenomenon has a positive impact on improving the electrochemical reactivity of the material[54]. In addition, the analysis of the d orbital partial DOS revealed that the d-band center of the FeS-ZnS/PCFs model (-2.783 eV) shifts upwards in comparison

Table 1. Comparison of ZnS-based materials for lithium storage properties

Samples	Current density (mA g^{-1})	Cycle number	Capacity (mAh g^{-1})	Ref.
FeS-ZnS/PCFs-20%	1,000	500	881.9	This work
ZnS-C/G	1,000	120	571.0	[8]
ZnS/CFs	1,000	500	602.2	[11]
ZnS/SnS@C	1,000	500	598.9	[12]
ZCS@NC@MS	1,000	500	448.0	[18]
ZnS/NC	1,000	500	420.0	[23]
ZnS@HPC	1,000	200	408.0	[28]
Ti-doped ZnS	1,000	500	463.1	[50]
ZnO@ZnS	200	100	513.4	[51]

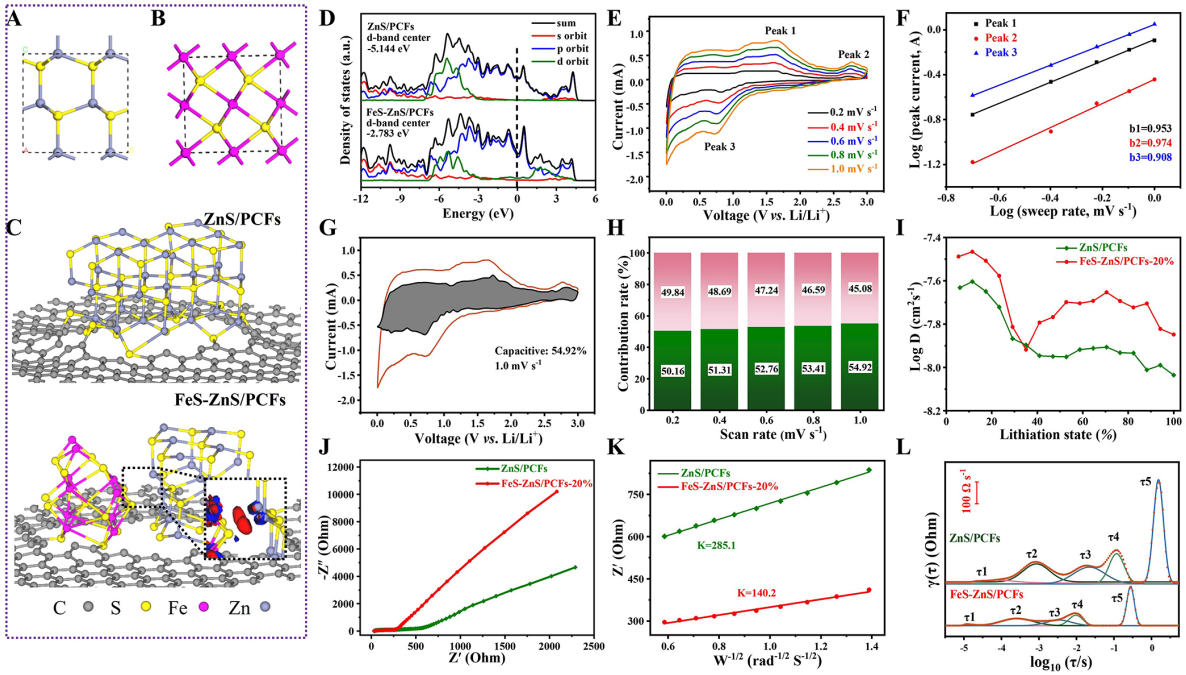

Figure 4. (A) Crystal structure model of FeS; (B) Crystal structure model of ZnS; (C) Theoretical calculation model; (D) Partial density of states (PDOS) of ZnS/PCFs and FeS-ZnS/PCFs-20%; (E) CV curves of the FeS-ZnS/PCFs-20% anode at various scan rates; (F) Corresponding *b* value fitting using the relationship between peak current and scan rate; (G) CV curves with capacitive contribution at 1.0 mV s^{-1}; (H) Contribution ratio *vs.* scan rate; (I) Corresponding Li-ion diffusion coefficient of the ZnS/PCFs and FeS-ZnS/PCFs-20% anodes; (J) EIS spectra of the ZnS/PCFs and FeS-ZnS/PCFs-20% anode; (K) linear fitting of the Warburg impedance of the ZnS/PCFs and FeS-ZnS/PCFs-20% anode; (L) DRT of the ZnS/PCFs and FeS-ZnS/PCFs-20% anodes.

to that of the ZnS/PCFs model (-5.144 eV). This upward shift is advantageous for the adsorption of ions on the surface[55]. The DFT calculation results are consistent with the experimental characterization and electrochemical performance testing stated previously. This not only provides a deeper theoretical comprehension for the research, but also suggests prospective benefits in the speed at which lithium is stored for FeS-ZnS/PCFs.

To investigate the lithium storage kinetics in the composite, CV measurements were conducted on the FeS-ZnS/PCFs-20% anode. The scan rates varied from 0.2 to 1 mV s^{-1}, as depicted in Figure 4E. With increasing scan rates, the reduction peak potential of FeS-ZnS/PCFs-20% shifted towards the negative side, and the

oxidation peak potential moved slightly towards the positive side. The results demonstrate that the lithium storage kinetics of FeS-ZnS/PCFs-20% exhibit good reversibility. The equation $i = av^b$ is used to determine the apparent current type during a lithium storage cycle. The exponent value of b represents the correlation between the current and the scan rate. It indicates the degree of capacitive or diffusion control in the system. A b-value of 1 indicates complete capacitance control, while a b-value of 0.5 indicates complete diffusion control[56]. The b-values measured at the oxidation or reduction peak potentials are 0.953, 0.974, and 0.908, as shown in Figure 4F. The data suggest that the material exhibits a capacitive-controlled characteristic near the redox peak potential. The extraordinary rate performance is mainly attributed to the increased adsorption of Li-ions at the surface contact. Moreover, it is feasible to determine the capacitive component of the specific capacity of the material for lithium storage. The shaded region in Figure 4G shows that the fitting result of FeS-ZnS/PCFs-20% indicates a capacitive contribution of 54.92% to the overall capacity when the scan rate is 1 mV s^{-1}. The value exceeds that of ZnS/PCFs (50.12%), as shown in Supplementary Figure 11. The aforementioned discovery offers additional proof of the synergistic impact arising from the well-suited and evenly distributed ZnS and FeS nanocrystals. The synergy between the components leads to the generation of additional active sites, enhancing the reactivity of lithium ions at both the surface and interface of the composite. Figure 4H illustrates the impact of the altering scan rate on the diffusion-controlled and capacitive-controlled contribution of FeS-ZnS/PCFs-20%. While the capacitive-controlled contribution does grow as the scan rate increases, the magnitude of this increase is not substantial. This confirms that the diffusion rate of Li-ions inside the bulk phases of the composite is likewise favorable.

Consequently, the diffusion coefficient of Li-ions (D_{Li+}) in the bulk phases of the samples was determined using the galvanostatic intermittent titration technique (GITT). The GITT curves produced for the discharge procedure are displayed in Supplementary Figure 12A. The determination of the apparent D_{Li+} in the active substance of the electrode can be achieved by utilizing the equation derived from Fick's second law (see Supplementary Materials)[57]. Figure 4I and Supplementary Figure 12B illustrate the variation in D_{Li+} while the active material of the electrode is undergoing lithiation upon discharge. Both samples exhibit a decline in D_{Li+} during the initial stages of lithium storage at high state of charge, which can be attributed to the challenge of Li-ion diffusion caused by the rapid initial lithium embedding[58]. As the level of charge falls, a significant quantity of Li ions diffuses slowly into the main part of the material, leading to the progressive stability of D_{Li+}. FeS-ZnS/PCFs-20% exhibits a higher D_{Li+} compared to ZnS/PCFs, indicating that the combined effect of ZnS and FeS not only enhances activity at the grain boundaries (as confirmed by XPS analysis), but also influences bonding and promotes the diffusion of Li-ions in the bulk phase.

Figure 4J displays the initial Nyquist plots obtained from the alternating current (AC) impedance measurements of ZnS/PCFs and FeS-ZnS/PCFs-20%. The Nyquist plot depicted in Supplementary Figure 13 corresponds to the corresponding circuit. Typically, the charge transfer resistance is reflected in the semicircles observed in the high-frequency region, while the Li-ion diffusion impedance is associated with the straight tails observed in the low-frequency region[59]. The lower interfacial resistance of FeS-ZnS/PCFs-20% is seen. In addition, a Warburg impedance (Z_w) analysis was conducted by fitting the impedance Z' in the low-frequency range to the reciprocal square root of the angular frequency ($\omega^{-1/2}$) using linear regression. The slope found, denoted as σ, corresponds to the Warburg factor, which is directly related to the D_{Li+}. The relevant formulas are as follows[3]:

$$Z' = R_{ct} + R_s + \sigma\omega^{-1/2} \quad (1)$$

$$D = R^2T^2/(2A^2n^4F^4C_{Li}\sigma^2) \quad (2)$$

where R is the gas constant (8.314 J K^{-1}), *T* is the absolute temperature (298 K), A is the surface area of the electrode, n is the electrons number per molecule in intercalation process, F is the Faraday constant (96,485 C mol^{-1}), C_{Li} is the Li-ions molar concentration in electrode, ω is the angular frequency, and σ is the Warburg factor related to Z′. The fitting results in Figure 4K show that FeS-ZnS/PCFs-20% has a σ value of 140.2, lower than that of ZnS/PCFs (285.1), thus demonstrating superior Li-ion diffusion performance, as previously found[60,61].

Finally, to enhance the understanding of the electrode processes, the Distribution of Relaxation Times (DRT) technique was utilized to elucidate distinct electrochemical processes. The DRT technique extracts the time constants g(τ) for each process from the collected electrochemical impedance spectroscopy (EIS) data. The corresponding formula is as follows[60,61]:

$$Z_{pol}(w)=\int_0^\infty \frac{g(\tau)}{1+jw\tau}d\tau \quad (3)$$

where τ is the relaxation time, g(τ) represents the DRT, j is an imaginary unit, and w is the angular frequency[54].

Thus, the overall polarization resistance can be expressed as the relaxation-dependent function g(τ). The relaxation duration signifies the electrochemical process that is linked to it, while the peak area that corresponds to it signifies the resistance of the sub-steps[62,63]. The findings of the DRT are displayed in Figure 4L. τ2 and τ3 represent the SEI impedance of the composite material and the counter electrode (lithium metal) in the half-cell, respectively[64,65]. The peaks at 10^{-1} to ten seconds (τ4 and τ5) represent the charge transfer processes, with τ5 often associated with the Li-ion intercalation process[63,66]. It is worth mentioning that the time constants for FeS-ZnS/PCFs-20% are consistently shorter than those for ZnS/PCFs, indicating that the target sample demonstrates an extraordinarily rapid electrochemical reaction. This can be attributed to the composite structure of ZnS-FeS.

The unique structure and multi-metal compound composition of the FeS-ZnS/PCFs-20% composite make it highly suitable for practical applications in full-cell LIBs[67,68]. To assess its performance, we constructed a full-cell LIB using FeS-ZnS/PCFs-20% as the anode and commercial lithium iron phosphate (LFP) as the cathode. Cycling tests, as depicted in Supplementary Figure 14, reveal that after 50 cycles at a current of 0.2 A g^{-1} within a voltage range of 0.5-3.9 V, the charging capacity of the FeS-ZnS/PCFs-20%//LFP battery remained stable at 183.6 mAh g^{-1}, with a Coulombic efficiency of approximately 87.6%. These findings underscore the considerable potential of FeS-ZnS/PCFs-20% as a promising anode material for LIBs.

CONCLUSIONS

Using a straightforward electrospinning process, we were able to successfully create FeS-ZnS/PCFs composites with porous architectures in this study. By modifying the quantity of iron acetylacetonate, we improved the lithium storage capacity of the composite. The FeS-ZnS/PCFs-20% anode demonstrated outstanding lithium storage capabilities, retaining a specific capacity of 881.9 mAh g^{-1} after 500 cycles at a current density of 1 A g^{-1}. The improved lithium storage capabilities of the FeS-ZnS/PCFs-20% anode arise from the combined effects of FeS and ZnS, which lead to greater redox activity, increased reaction sites on the surface interface, and improved asynchronous lithium storage properties. Moreover, the exceptional electrochemical performance of FeS-ZnS/PCFs-20% is supported by DFT calculations and data on the

kinetics of lithium storage. This study can provide new insights for designing and preparing a range of composites tailored for high-performance LIB anodes.

DECLARATIONS

Authors' contributions

Conceptualization: Wang, W.
Writing - original draft preparation, validation: Tang, H.
Investigation: Cunha, J.
Supervision, resources: Karimi, M.
Visualization:·Lashari, N.
Investigation, visualization: Ahmad, A.
Project administration, review & editing: Yin, H.

Availability of data and materials

Data will be made available upon request from the author.

Financial support and sponsorship

This research is supported by the National Natural Science Foundation of China (Grant Nos. 52271211), the Science and Technology Innovation Program of Hunan Province (Grant No. 2023RC3185), the EU HORIZON Marie Skłodowska-Curie Actions-2021-PF (No. 101065098), and the European Research Executive Agency (Project 101079184-FUNLAYERS).

Conflicts of interest

All authors declared that there are no conflicts of interest.

Ethical approval and consent to participate

Not applicable.

Consent for publication

Not applicable.

REFERENCES

1. Wang, W.; Wang, H.; Wu, Z.; et al. Co/MnO/N-C hybrid derived from N-methyl-D-glucamine as efficient bifunctional oxygen electrocatalysts. *Electrochim. Acta.* **2018**, *281*, 486-93. DOI
2. Yin, H.; Li, H.; Zhao, H.; et al. SnSe nanoplates swallowed in carbon nanofibers as the self-standing anode for lithium-ion and sodium batteries with enhanced performance. *Int. J. Hydrogen. Energy.* **2023**, *48*, 4789-99. DOI
3. Cruz-Manzo, S.; Greenwood, P. An impedance model based on a transmission line circuit and a frequency dispersion Warburg component for the study of EIS in Li-ion batteries. *J. Electroanal. Chem.* **2020**, *871*, 114305. DOI
4. He, B.; Cunha, J.; Hou, Z.; Li, G.; Yin, H. 3D hierarchical self-supporting Bi_2Se_3-based anode for high-performance lithium/sodium-ion batteries. *J. Colloid. Interface. Sci.* **2023**, *650*, 857-64. DOI
5. Zhou, Y.; Wang, C.; Chen, F.; et al. Synchronous constructing ion channels and confined space of Co_3O_4 anode for high-performance lithium-ion batteries. *Nano. Res.* **2022**, *15*, 6192-9. DOI
6. Wen, L.; Cheng, F.; Wang, X.; et al. Recent advances of cobalt-free and nickel-rich cathode materials for lithium-ion batteries. *Energy. Mater.* **2024**, *4*, 400054. DOI
7. Fu, S.; Yang, X.; Zhao, P.; Yao, X.; Jiao, Z.; Cheng, L. Regulable electron transfer on ZnS/CoS_2/CC prepared by an MOF-on-MOF strategy for robust LIB performance. *ACS. Appl. Energy. Mater.* **2022**, *5*, 5159-69. DOI
8. Tian, G.; Zhao, Z.; Sarapulova, A.; et al. Understanding the Li-ion storage mechanism in a carbon composited zinc sulfide electrode. *J. Mater. Chem. A.* **2019**, *7*, 15640-53. DOI

9. Li, H.; Luo, J.; Han, D.; et al. Layer-by-layer hetero-carbon modifying ZnS nanocubes anode with improved long-term life for sodium-ion batteries. *Ceram. Int.* **2023**, *49*, 18421-31. DOI
10. Wang, J.; Yao, J.; Li, W.; et al. Lithium molybdate composited with carbon nanofibers as a high-capacity and stable anode material for lithium-ion batteries. *Energy. Mater.* **2022**, *2*, 200026. DOI
11. Wang, W.; Guan, M.; Wang, Q.; et al. In situ embedment of ZnS nanocrystals in high porosity carbon fibers as an advanced anode material for efficient lithium storage. *Acta. Metall. Sin.* **2023**, *36*, 167-76. DOI
12. Zhang, L.; Zhang, M.; Peng, F.; et al. Rationally designed heterostructure ZnS/SnS@N-doped carbon microspheres as high-performance anode for lithium-ion batteries. *J. Alloys. Compd.* **2022**, *910*, 164908. DOI
13. He, F.; Wang, Y.; Liu, J.; Yao, X. One-dimensional carbon based nanoreactor fabrication by electrospinning for sustainable catalysis. *Exploration* **2023**, *3*, 20220164. DOI PubMed PMC
14. Zan, G.; Li, S.; Chen, P.; Dong, K.; Wu, Q.; Wu, T. Mesoporous cubic nanocages assembled by coupled monolayers with 100% theoretical capacity and robust cycling. *ACS. Cent. Sci.* **2024**, *10*, 1283-94. DOI PubMed PMC
15. Ni, X.; Cui, Z.; Jiang, N.; et al. Hollow multi-nanochannel carbon nanofiber/MoS_2 nanoflower composites as binder-free lithium-ion battery anodes with high capacity and ultralong-cycle life at large current density. *J. Mater. Sci. Technol.* **2021**, *77*, 169-77. DOI
16. Li, Z.; Yin, Q.; Hu, W.; et al. Tin/tin antimonide alloy nanoparticles embedded in electrospun porous carbon fibers as anode materials for lithium-ion batteries. *J. Mater. Sci.* **2019**, *54*, 9025-33. DOI
17. Zhao, S.; Sewell, C. D.; Liu, R.; et al. SnO_2 as advanced anode of alkali-ion batteries: Inhibiting sn coarsening by crafting robust physical barriers, void boundaries, and heterophase interfaces for superior electrochemical reaction reversibility. *Adv. Energy. Mater.* **2020**, *10*, 1902657. DOI
18. Guan, B.; Sheng, L.; Zhang, N.; et al. Bimetallic metal-organic framework derived transition metal sulfide microspheres as high-performance lithium/sodium storage materials. *Chem. Eng. J.* **2022**, *446*, 137154. DOI
19. Ma, Z.; Shi, J.; Wu, D.; et al. Sn-doped thioantimonate superionic conductors with high air stability and enhanced Li-ion conduction for all-solid-state lithium batteries. *J. Mater. Chem. A.* **2023**, *11*, 23342-53. DOI
20. Zhang, J.; Wang, Y.; Xia, Q.; et al. Confining polymer electrolyte in MOF for safe and high-performance all-solid-state sodium metal batteries. *Angew. Chem. Int. Ed.* **2024**, *63*, e202318822. DOI
21. Xie, D.; Cai, S.; Sun, X.; et al. FeS/ZnS nanoflower composites as high performance anode materials for sodium ion batteries. *Inorg. Chem. Commun.* **2020**, *111*, 107635. DOI
22. Zhao, L. P.; Meng, W. S.; Wang, H. Y.; Qi, L. MoS_2-C composite as negative electrode material for sodium-ion supercapattery. *Acta. Phys. Chim. Sin.* **2017**, *33*, 787-94. DOI
23. Wang, P.; Jiang, Y.; Cao, Y.; Wu, X.; Liu, X. MOF-derived ZnS/NC yolk-shell composites for highly reversible lithium storage. *New. J. Chem.* **2022**, *46*, 11101-7. DOI
24. Fan, H. H.; Li, H. H.; Guo, J. Z.; et al. Target construction of ultrathin graphitic carbon encapsulated FeS hierarchical microspheres featuring superior low-temperature lithium/sodium storage properties. *J. Mater. Chem. A.* **2018**, *6*, 7997-8005. DOI
25. Qiu, X.; Yu, Y.; Peng, Z.; et al. Cobalt sulfides nanoparticles encapsulated in N, S co-doped carbon substrate for highly efficient oxygen reduction. *J. Alloys. Compd.* **2020**, *815*, 152457. DOI
26. Li, Z.; Wang, W.; Zhou, M.; et al. *In-situ* self-templated preparation of porous core-shell Fe_{1-S}@N, S co-doped carbon architecture for highly efficient oxygen reduction reaction. *J. Energy. Chem.* **2021**, *54*, 310-7. DOI
27. Yin, H.; Jia, L.; Li, H. Y.; et al. Point-cavity-like carbon layer coated SnS nanotubes with improved energy storage capacity for lithium/sodium ion batteries. *J. Energy. Storage.* **2023**, *65*, 107354. DOI
28. Chen, H.; Zhang, B.; Cao, Y.; et al. ZnS nanoparticles embedded in porous honeycomb-like carbon nanosheets as high performance anode material for lithium ion batteries. *Ceram. Int.* **2018**, *44*, 13706-11. DOI
29. Zhou, J.; Lian, J.; Hou, L.; et al. Ultrahigh volumetric capacitance and cyclic stability of fluorine and nitrogen co-doped carbon microspheres. *Nat. Commun.* **2015**, *6*, 8503. DOI PubMed PMC
30. Ma, Q.; Zhuang, Q.; Liang, J.; et al. Novel mesoporous flowerlike iron sulfide hierarchitectures: facile synthesis and fast lithium storage capability. *Nanomaterials* **2017**, *7*, 431. DOI PubMed PMC
31. Wang, W.; Gong, J.; Long, Q.; et al. Fe-Fe_3N composite nitrogen-doped carbon framework: multi-dimensional cross-linked structure boosting performance for the oxygen reduction reaction electrocatalysis and zinc-air batteries. *Appl. Surf. Sci.* **2023**, *639*, 158218. DOI
32. Shao, M.; Cheng, Y.; Zhang, T.; et al. Designing MOFs-derived FeS_2@carbon composites for high-rate sodium ion storage with capacitive contributions. *ACS. Appl. Mater. Interfaces.* **2018**, *10*, 33097-104. DOI
33. Lee, G. J.; Chen, H. C.; Wu, J. J. Enhancing the photocatalytic hydrogen evolution of copper doped zinc sulfide nanoballs through surfactants modification. *Int. J. Hydrogen. Energy.* **2019**, *44*, 30563-73. DOI
34. Zhang, Y.; Wang, P.; Yin, Y.; et al. Heterostructured SnS-ZnS@C hollow nanoboxes embedded in graphene for high performance lithium and sodium ion batteries. *Chem. Eng. J.* **2019**, *356*, 1042-51. DOI
35. Wei, Y.; Bai, W.; Yu, S.; Wang, Z.; Wang, J. Engineering hierarchical structure of multi-phase metal sulfides with doped carbon protector towards superb energy storage. *Appl. Surf. Sci.* **2022**, *600*, 154155. DOI
36. Li, J.; Yan, D.; Zhang, X.; et al. ZnS nanoparticles decorated on nitrogen-doped porous carbon polyhedra: a promising anode material for lithium-ion and sodium-ion batteries. *J. Mater. Chem. A.* **2017**, *5*, 20428-38. DOI
37. Yin, H.; He, J.; Xiao, B.; et al. Advances and prospects of g-C_3N_4 in lithium-sulfur batteries. *Nano. Res. Energy.* **2024**, *3*, e9120138. DOI

38. Qin, W.; Li, D.; Zhang, X.; Yan, D.; Hu, B.; Pan, L. ZnS nanoparticles embedded in reduced graphene oxide as high performance anode material of sodium-ion batteries. *Electrochim. Acta.* **2016**, *191*, 435-43. DOI
39. Ho, S. F.; Yang, Y. C.; Tuan, H. Y. Silver boosts ultra-long cycle life for metal sulfide lithium-ion battery anodes: taking $AgSbS_2$ nanowires as an example. *J. Colloid. Interface. Sci.* **2022**, *621*, 416-30. DOI PubMed
40. Xiao, F.; Yuan, D.; Zhu, S.; Zhu, J. Ni-Co sulfide electrode material for supercapacitor. *J. Funct. Mater.* **2017**, *48*, 9001-6. DOI
41. Wei, X.; Li, W.; Shi, J. A.; Gu, L.; Yu, Y. FeS@C on carbon cloth as flexible electrode for both lithium and sodium storage. *ACS. Appl. Mater. Interfaces.* **2015**, *7*, 27804-9. DOI
42. Fei, L.; Lin, Q.; Yuan, B.; et al. Reduced graphene oxide wrapped FeS nanocomposite for lithium-ion battery anode with improved performance. *ACS. Appl. Mater. Interfaces.* **2013**, *5*, 5330-5. DOI
43. Wang, L.; Ju, J.; Deng, N.; Wang, G.; Cheng, B.; Kang, W. ZnS nanoparticles anchored on porous carbon nanofibers as anode materials for lithium ion batteries. *Electrochem. Commun.* **2018**, *96*, 1-5. DOI
44. Huang, M.; Xu, A.; Duan, H.; Wu, S. Enhanced pseudocapacitance contribution to outstanding Li-storage performance for a reduced graphene oxide-wrapped FeS composite anode. *J. Mater. Chem. A.* **2018**, *6*, 7155-61. DOI
45. Zhang, B.; Xia, G.; Sun, D.; Fang, F.; Yu, X. Magnesium hydride nanoparticles self-assembled on graphene as anode material for high-performance lithium-ion batteries. *ACS. Nano.* **2018**, *12*, 3816-24. DOI
46. Kerkar, R. D.; Salker, A. V. Synergistic effect of modified Pd-based cobalt chromite and manganese oxide system towards NO-CO redox detoxification reaction. *Environ. Sci. Pollut. Res. Int.* **2020**, *27*, 27061-71. DOI PubMed
47. Hou, Y. L.; Chen, J. Z.; Zhang, B. H.; Wang, H. Y.; Wen, W. X.; Zhao, D. L. Fast ion/electron transport enabled by MXene confined bimetallic sulfides with heterostructure toward highly effective lithium/sodium storage. *Chem. Eng. J.* **2024**, *479*, 147914. DOI
48. Ji, H.; Ji, W.; Xue, H.; et al. Synergistic activation of anionic redox via cosubstitution to construct high-capacity layered oxide cathode materials for sodium-ion batteries. *Sci. Bull.* **2023**, *68*, 65-76. DOI
49. Zhou, J. Theoretical design of a novel 2D tetragonal ZnS/SnO hetero-bilayer as a promising photocatalyst for solar water splitting. *Int. J. Hydrogen. Energy.* **2019**, *44*, 27816-24. DOI
50. Jiang, H.; Zeng, Y.; Zhang, J.; et al. High-performance Ti-doped ZnS thin film anode for lithium-ion batteries. *Nanotechnology* **2022**, *33*, 455402. DOI
51. Li, H.; Wang, J.; Zhao, Y.; Tan, T. Synthesis of the ZnO@ZnS nanorod for lithium-ion batteries. *Energies* **2018**, *11*, 2117. DOI
52. Ferahtia, S.; Saib, S.; Bouarissa, N. Computational studies of mono-chalcogenides ZnS and ZnSe at high-pressures. *Results. Phys.* **2019**, *15*, 102626. DOI
53. Yin, S.; Bernstein, E. R. Properties of iron sulfide, hydrosulfide, and mixed sulfide/hydrosulfide cluster anions through photoelectron spectroscopy and density functional theory calculations. *J. Chem. Phys.* **2016**, *145*, 154302. DOI PubMed
54. Rao, Y.; Kong, F.; Zheng, Y.; et al. Order-disorder transition mechanism for high-capacity amorphous anodes of lithium-ion batteries. *Renew. Sustain. Energy. Rev.* **2022**, *165*, 112613. DOI
55. Jiao, S.; Fu, X.; Huang, H. Descriptors for the evaluation of electrocatalytic reactions: d-band theory and beyond. *Adv. Funct. Mater.* **2022**, *32*, 2107651. DOI
56. Chen, Y.; Hu, X.; Evanko, B.; et al. High-rate FeS_2/CNT neural network nanostructure composite anodes for stable, high-capacity sodium-ion batteries. *Nano. Energy.* **2018**, *46*, 117-27. DOI
57. Ding, S.; Petuskey, W. T. Solutions to fick's second law of diffusion with a sinusoidal excitation. *Solid. State. Ion.* **1998**, *109*, 101-10. DOI
58. Zhang, W.; Zheng, S.; Ma, T.; Sun, T.; Tao, Z. Hollow tubular conjugated organic polymer for lithium batteries. *Nano. Res.* **2023**, *16*, 2474-9. DOI
59. Sheng, Q.; Li, Q.; Xiang, L.; Huang, T.; Mai, Y.; Han, L. Double diamond structured bicontinuous mesoporous titania templated by a block copolymer for anode material of lithium-ion battery. *Nano. Res.* **2021**, *14*, 992-7. DOI
60. Huang, J.; Sullivan, N. P.; Zakutayev, A.; O'hayre, R. How reliable is distribution of relaxation times (DRT) analysis? A dual regression-classification perspective on DRT estimation, interpretation, and accuracy. *Electrochim. Acta.* **2023**, *443*, 141879. DOI
61. Xia, J.; Wang, C.; Wang, X.; Bi, L.; Zhang, Y. A perspective on DRT applications for the analysis of solid oxide cell electrodes. *Electrochim. Acta.* **2020**, *349*, 136328. DOI
62. Brown, D. E.; Mcshane, E. J.; Konz, Z. M.; Knudsen, K. B.; Mccloskey, B. D. Detecting onset of lithium plating during fast charging of Li-ion batteries using operando electrochemical impedance spectroscopy. *Cell. Rep. Phys. Sci.* **2021**, *2*, 100589. DOI
63. Wang, M.; Wang, J.; Xiao, J.; et al. Introducing a pseudocapacitive lithium storage mechanism into graphite by defect engineering for fast-charging lithium-ion batteries. *ACS. Appl. Mater. Interfaces.* **2022**, *14*, 16279-88. DOI
64. Effat, M. B.; Ciucci, F. Bayesian and hierarchical bayesian based regularization for deconvolving the distribution of relaxation times from electrochemical impedance spectroscopy data. *Electrochim. Acta.* **2017**, *247*, 1117-29. DOI
65. Xue, L.; Li, Y.; Lin, W.; Chen, F.; Chen, G.; Chen, D. Electrochemical properties and facile preparation of hollow porous V_2O_5 microspheres for lithium-ion batteries. *J. Colloid. Interface. Sci.* **2023**, *638*, 231-41. DOI
66. Rüther, T.; Schamel, M.; Plank, C.; Schomburg, F.; Röder, F.; Danzer, M. A. Cell-to-cell variation beyond parameter analysis-identification and correlation of processes in lithium-ion batteries using a combined distribution of relaxation times analysis. *J. Power. Sources.* **2023**, *587*, 233677. DOI
67. Wang, K.; Huang, J.; Chen, H.; et al. Recent progress in high entropy alloys for electrocatalysts. *Electrochem. Energy. Rev.* **2022**, *5*, 17. DOI
68. Li, W.; Guo, Z.; Yang, J.; et al. Advanced strategies for stabilizing single-atom catalysts for energy storage and conversion. *Electrochem. Energy. Rev.* **2022**, *5*, 9. DOI